CHEMISTRY OF MATERIALS

ARTICLE

pubs.acs.org/cm

Amorphous Iron Oxide Decorated 3D Heterostructured Electrode for Highly Efficient Oxygen Reduction

Wei Zhou,[†] Lei Ge,[†] Zhi-Gang Chen,[‡] Fengli Liang,[†] Hong-Yi Xu,[‡] Julius Motuzas,[§] Anne Julbe,[§] and Zhonghua Zhu*[,†]

[†]School of Chemical Engineering and [‡]School of Materials Engineering and Centre for Microscopy and Microanalysis, University of Queensland, Brisbane, Queensland 4072, Australia

[§]Institut Européen des Membranes, Universite Montpellier 2 (CC 47), Place Eugene Bataillon, 34095 Montpellier Cedex 5, France

Supporting Information

ABSTRACT: Low-temperature reduction of oxygen with high efficiency is required for widespread application of electrochemical devices. Noble metal catalysts are favored for use as the surface modifier on ceramic electrodes to enhance their oxygen reduction reactivity. However, the disadvantages of noble metals, such as sintering and high price, restrict their practical applications. Here, we present a 5-nm-thick amorphous iron oxide thin film decorated electrode possessing not only high electrocatalytic activity comparable to that of the platinum (Pt) modified one but also improved stability. The iron oxide is deposited into porous perovskite $SrSc_{0.2}Co_{0.8}O_{3-\delta}$ (SSC) by chemical vapor deposition (CVD), forming a three-dimensional (3D) heterostructured electrode using ferrocene as the precursor. The importance of CVD is not only ensuring the uniform distribution of iron oxide but also allowing the iron oxide to be amorphous. At 700 °C, the area specific resistance (ASR) of the 3D heterostructured cathode is reduced to 0.01 Ω cm^2, which is only 50% of that of the unmodified one, and the derived single fuel cell achieves higher power delivery. The electrode operates stably at 650 °C for 250 h without any degradation, while the performance of Pt modified SSC starts to degrade only after 30 min. These results suggest that amorphous iron oxide can be used as the catalyst to improve oxygen reduction reaction (ORR), with the benefits of long-lifetime and low cost.

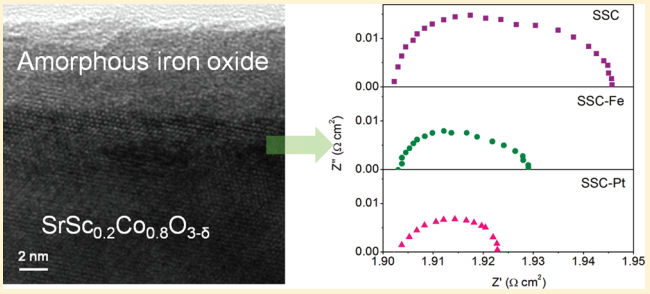

KEYWORDS: electrochemistry, fuel cells, perovskite, heterostructure, amorphous iron oxide

INTRODUCTION

Intermediate-temperature solid oxide fuel cells (IT-SOFCs) operating between 600 and 750 °C are gaining increasing attention.[1] In this temperature range, problems with seals and long-term electrode stability would be solved, so the SOFC can be suitable for smaller-scale applications with a larger mass market. The main barrier to achieving acceptable chemical-to-electrical conversion efficiency in IT-SOFCs is the sluggish oxygen reduction reaction (ORR) kinetics on the cathode.[2]

Fabrication of electrodes by infiltration has provided a new approach to improve the performance and stability of cathodes for IT-SOFCs.[3] Nanostructured catalyst modified composite cathodes can be obtained by infiltrating a metal ions solution into a ceramic scaffold, followed by heating at high temperature. Noble metal catalysts, such as Pt and Pd, show superior performance for ORR at lower operation temperature,[3b] but they are not favorable for the practical application as a result of their easy sintering behavior and high price.

Cobalt and iron-based catalysts, such as Fe−N_4 and Co−N_4, have been explored to catalyze ORR for polymer electrolyte membrane fuel cells (PEMFCs).[4] Because the operation temperature for these catalysts is below 100 °C, their application for SOFCs is restrained. The cobalt oxide was reported as a promoter for ORR in the cathode of SOFCs. However, cobalt is still 10 times more expensive than iron.[5] The use of iron oxide as the electrocatalyst in fuel cells is rarely reported likely because of the negligible activity of crystallized iron oxide on ORR. It is supported by the fact that the decoration of crystallized Fe_2O_3 leads to deteriorated electrocatalytic activity on ORR (Figure S1 in the Supporting Information).

Herein, we report for the first time a novel 3D heterostructured electrode (SSC-Fe) decorated by amorphous iron oxide that works stably at 650 °C, with oxygen reduction reactivity comparable to that of a Pt decorated one. The importance of CVD is not only ensuring the uniform distribution of iron oxide but also allowing the iron oxide to be amorphous.

Received: May 22, 2011
Revised: August 3, 2011
Published: August 19, 2011

dx.doi.org/10.1021/cm201439d | *Chem. Mater.* 2011, 23, 4193–4198

EXPERIMENTAL SECTION

Synthesis and Preparation. SSC was synthesized by a combined EDTA-citrate complexing process. $Sr(NO_3)_2$, $Co(NO_3)_2 \cdot xH_2O$, and Sc_2O_3 were applied as the raw materials for the metal ion sources. The necessary amount of Sc_2O_3 was weighed and dissolved in the HNO_3 aqueous solution under heating; $Sr(NO_3)_2$ solid and $Co(NO_3)_2$ aqueous solution were added at the required stoichiometry, followed by the introduction of EDTA and citric acid as complexing agents. The pH value of the system was controlled at ~6 with the help of $NH_3 \cdot H_2O$. After the evaporation of the water under heating, a transparent purple gel was obtained and then preheated at 250 °C to form a solid precursor; this was followed by the calcining of the precursor at 850 °C in air for 5 h to get the SSC powders.

The SSC scaffold was prepared by the wet powder spraying method. The SSC slurry for spray deposition was prepared by dispersing SSC powder in a premixed solution of glycerol and isopropyl alcohol, followed by rapid mixing and milling in an agate mortar for 0.5 h. A symmetrical cell of electrode|$Sm_{0.2}Ce_{0.8}O_{1.9}$ (SDC)|electrode configuration was fabricated by spraying the SSC slurry onto both surfaces of a SDC disk in a symmetric configuration and calcining the sprayed cells in air at 1000 °C for 2 h.

The anode substrates were prepared by a tape casting process. The slurry for the tape casting process was prepared by two step ball milling. NiO, yttria stabilized zirconia (YSZ), and starch were ball milled with organic solvent in an agate jar for 24 h using triethanolamine as the surfactant. Subsequently, polyvinyl butyral (PVB), polyethylene glycol (PEG), and dibutyl o-phthalate (DOP) were added as the binder and two plasticizers, respectively, followed by ball milling for another 24 h to form the slurry. The slurry was vacuum pumped under 200 mbar (absolute) to remove air and then cast onto the polymer carrier on a tape casting machine. The tape was dried under ambient conditions for 24 h, and then, it was detached from the polymer carrier. A circular anode substrate with a 16 mm diameter was drilled from the tape by a punch, followed by presintering at 1150 °C in air to remove organic residues. The SDC|YSZ double electrolyte layers were prepared via wet powder spraying. The YSZ and SDC suspensions were sprayed onto the anode substrate in sequence using a spraying gun with a nozzle size of 0.35 mm (diameter). Nitrogen was used as the carrier gas at a working pressure of 1 atm. The spraying gun was aligned vertically to the anode substrate, leaving a 10 mm distance between them. The spray speed was controlled at about 0.005 g s^{-1} (YSZ or SDC). The spray process was carried out at a substrate temperature of ~200 °C with the help of a hot plate. After the spray deposition, the green triple-layer pellets were fired at 1450 °C in air for 5 h at a heating rate of 3 °C min^{-1}. The BSF slurry was then painted onto the center of the disk electrolyte and fired at 1000 °C for 2 h in air. The resulting coin-shaped film cathode had a thickness of 10−20 μm and an area of 0.48 cm^2.

The amorphous iron oxide was deposited on the surface of the SSC scaffold via CVD using ferrocene ($Fe(C_5H_5)_2$) as iron precursor. Ferrocene was gasified and decomposed at 600 °C in a horizontal quartz tube housed in a cylindrical furnace; meanwhile, an argon flow carried the gasified ferrocene toward the center of the furnace, where metallic iron particles were deposited into the porous SSC layer.

Characterization. A pananalytical X-Pert Pro X-ray apparatus with an in situ heating accessory (HT-XRD, HT1200) and Cu Kα radiation was utilized to determine the structural evolution of powders during the temperature cycle from 100 to 900 °C in air with a heating rate of 5 °C min^{-1}. The sample was stabilized by leaving it for 10 min at the target temperature before each analysis. Le Bail refinements on the X-ray diffraction(XRD) patterns were carried out using DIFFRAC^{plus} TOPAS 4.2 software. During the refinements, general parameters, such as the scale factor, background parameters, and the zero point of the counter, were optimized.

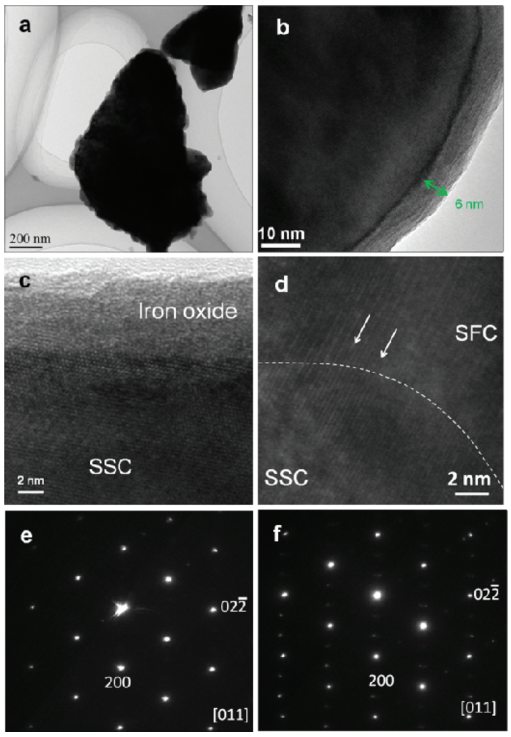

Figure 1. TEM images of amorphous iron oxide decorated SSC: (a) typical TEM image of an SSC-Fe particle; (b and c) HRTEM images of the amorphous layer; (d) HRTEM image at the interface between the two phases, showing epitaxial growth of SFC on SSC; (e) SAED image of the bulk of the SSC, showing a single cubic phase; and (f) SAED image of the outer portion of the SSC, indicating the existence of superstructure.

Fourier transform infrared spectroscopy (FT-IR; Model Nicolet AVATAR-360) of the SSC-Fe powders was recorded from 4000 to 400 cm^{-1} by the KBr pellet method.

The chemical state of iron in SSC-Fe was analyzed using a Kratos Axis ULTRA X-ray photoelectron spectrometer, incorporating a 165 mm hemispherical electron energy analyzer. The incident radiation was monochromatic Al Kα X-rays (1486.6 eV) at 150 W (15 kV, 15 mA). Narrow high-resolution scans were run to obtain Fe 2p level spectra with 0.05 eV steps and 250 ms dwell time. The base pressure in the analysis chamber was 1.0×10^{-9} Torr, and during sample analysis, it was 1.0×10^{-8} Torr. All binding energies were referenced to the C 1s peak (285 eV) arising from adventitious carbon.

Thermal gravimetric (TG) and differential thermal analysis (DTA) curves in air were simultaneously obtained in a TGA-DSC apparatus 2960 SDT V3.0F. Analyses were carried out under the air flow rate 20 mL min^{-1}, between room temperature and 900 °C, and at the ramping and cooling rate 2 °C min^{-1}.

Transmission electron microscopy (TEM) was conducted at 200 kV with a Philips Tecnai T30F field emission instrument equipped with a 2k-CCD camera. Energy dispersive X-ray spectroscopy (EDS) was carried out by a light-element detector using the ZAF technique.

Electrochemical Measurements. The electrochemical impedance spectra (EIS) of the symmetric cells were obtained using an Autolab PGSTAT30 electrochemical workstation. The frequency range was 0.01 Hz to 100 kHz, and the signal amplitude was 10 mV under open cell voltage conditions. The coin-shaped fuel cell was mounted onto an alumina tube and sealed by ceramic paste at 150 °C before it was heated for testing. H_2 was fed into the anode side as a fuel at a flow rate of 60 mL min^{-1} (STP) while the cathode side was exposed to air.

dx.doi.org/10.1021/cm201439d |*Chem. Mater.* 2011, 23, 4193–4198

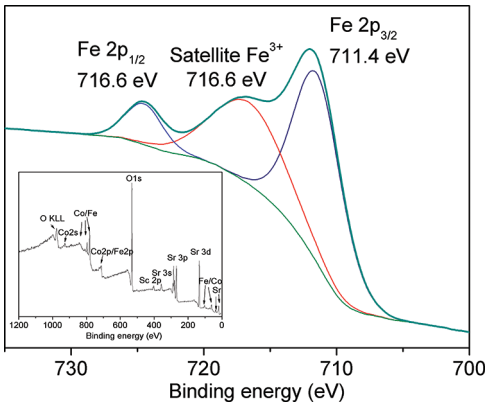

Figure 2. XPS spectroscopic data for the SSC-Fe fired at 800 °C.

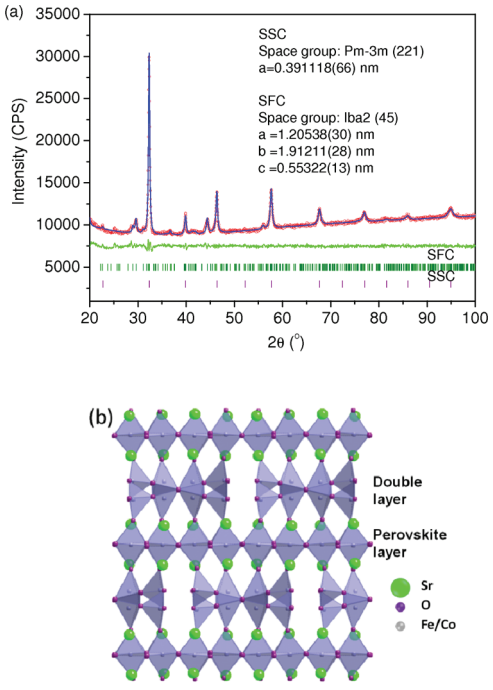

Figure 3. Structural analysis of the SSC-Fe. (a) Le Bail refined XRD pattern of SSC-Fe with experimental data (red dots), calculated profiles (blue line), difference curve (green line), and the calculated Bragg positions (vertical bar) for each phase. (b) Schematic representation of the orthorhombic SFC.

The current−voltage curves of the fuel cells operated between 600 and 750 °C were obtained using an Autolab PGSTAT30 electrochemical workstation. Electrodes and electrolyte polarization resistance were obtained from the EIS of the fuel cell obtained in the frequency range 0.01 Hz to 100 kHz with a signal amplitude of 50 mV under open circuit voltage (OCV).

RESULTS AND DISCUSSION

The infiltration method was first tried to fabricate iron oxide decorated SSC. The obtained iron oxide was crystallized, which is detrimental to the ORR (Figure S1 in the Supporting Information). The CVD method allows the iron oxide not only to deposit very uniformly on the surface of SSC but also to be at amorphous status. After calcinations at 800 °C for 5 h in air, as

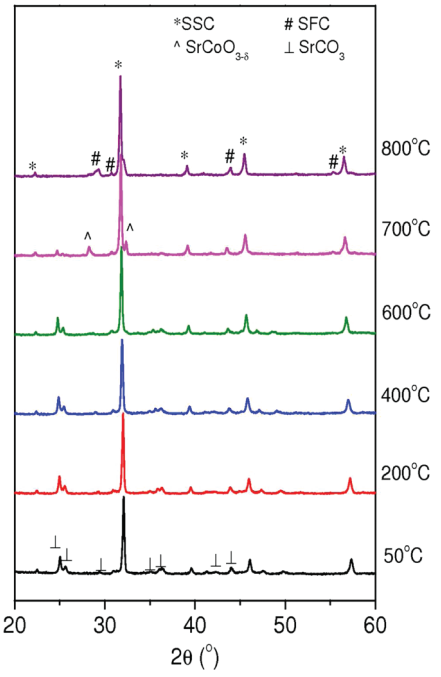

Figure 4. In-situ XRD tested between 50 and 800 °C.

compared with pristine SSC (Figure S2 in the Supporting Information), a thin film is coated on the SSC as illustrated in Figure 1. According to the high resolution transmission electron microscopy (HRTEM) image (Figure 1c), this film shows an amorphous morphology with thickness ~ 6 nm. The energy dispersive spectrometer (EDS) result shows that this thin film is enriched in iron. The CVD allows iron oxide to distribute finely on the SSC. The amorphicity of iron oxide is related to an ultrasmall dimension and "space restriction", leading to the absence of a periodic lattice.[6]

The valence state of iron in the film is studied by X-ray photoelectron spectroscopy (XPS) (Figure 2). The peak positions at 711.4 and 724.8 eV for Fe $2p_{3/2}$ and Fe $2p_{1/2}$ and a shakeup satellite at about 716.6 eV suggest the presence of Fe^{3+} in the film, but no characteristic peaks belonging to Fe_2O_3 or Fe_3O_4 can be observed by XRD (Figure 3a). This shows that the iron oxide is amorphous. In addition, a new phase is observed, which has a diffraction peak similar to that of the layer-structured $Sr_4Fe_6Co_{6-x}O_{13-\delta}$ (SFC).[7] Le Bail refinement carried out on XRD pattern confirms the existence of SFC and the main cubic phase SSC; the former is identified as an orthorhombic structure with the space group *Iba*2 (45) (Figure 3b). The refined lattice parameters are a = 12.0538(30) Å, b = 19.1211(28) Å, and c = 5.5322(13) Å. The refinements converge to reliability factors $\chi^2 = 1.30$, $R_p = 0.96$, $R_{wp} = 1.29$, $R_{exp} = 0.99$, and $R_{Bragg} = 0.174$. The relatively low reliability factor values indicate good fitting. The selected area electron diffraction (SAED) pattern (Figure 1f) further confirms the formation of superstructured SFC between SSC and amorphous iron oxide. No obvious change of the crystalline orientation between SSC and SFC can be observed by HRTEM, indicating that the SFC is an epitaxial growth on the SSC. Numerous reports have shown that the epitaxial thin film of a layered oxide growing on a two-dimensional (2D) flat substrate allows the highly improved oxygen diffusion rate.[8] Nevertheless, the integration of such thin films in whole devices is still a big challenge because of the extremely limited reaction area for the 2D flat structured

dx.doi.org/10.1021/cm201439d |*Chem. Mater.* 2011, 23, 4193–4198

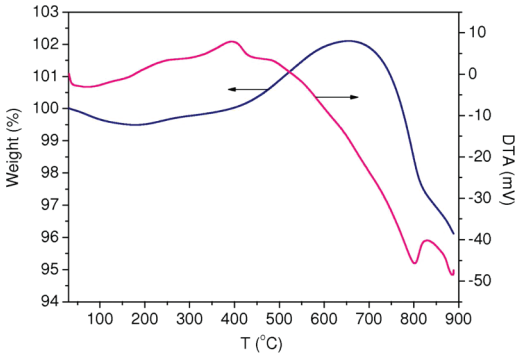

Figure 5. Thermal analysis curves of SSC-Fe recorded in air: TGA (left axis) and DTA (right axis).

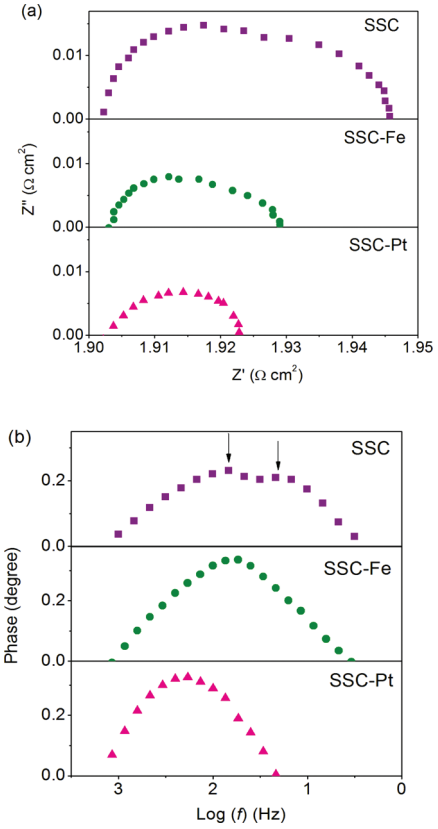

Figure 6. Electrochemical impedance spectroscopy of pristine SSC, SSC-Fe, and SSC-Pt cathodes. (a) Nyquist and (b) Bode curves of the cathodes tested by EIS in air at 650 °C.

electrode. In the present work, for the first time, we successfully prepared the epitaxial film into the porous perovskite scaffold, forming a 3D heterostructure.

The phase formation of the SFC was studied by in situ X-ray diffraction (XRD) (Figure 4). Metallic iron (JCPDS file No. 85-1410) is detected in the as-deposited SSC composite as expected. $SrCO_3$ (JCPDS file No. 05-0418) is also detected as a result of the reaction between SSC and CO_2. The CO_2 is likely formed from the catalytic oxidization of ferrocene on the surface of SSC, where the oxygen for this ferrocene oxidization is released from the SSC perovskite lattice at high temperature. It was reported that the CO_2 can react with Sr-containing perovskite

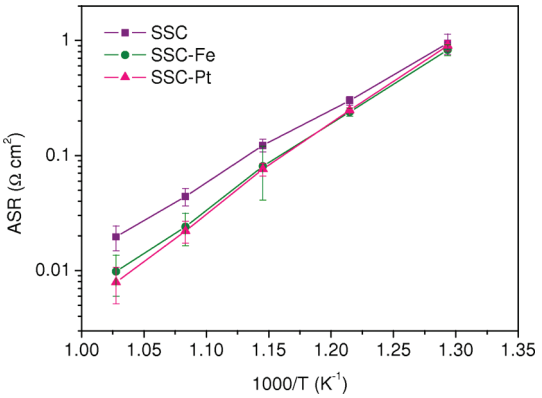

Figure 7. Comparison of the ASRs of the three cathodes by testing the EIS of symmetric cells.

to form carbonates in the temperature range 500−700 °C.[9] The carbonates may block the ORR on the cathode, thus leading to the dramatic degradation of cathode performance. In our study, however, with increasing temperature, the relative intensity of corresponding diffraction peaks of $SrCO_3$ starts to decrease at 700 °C and the peaks completely vanish at 800 °C. The absence of carbonate is also confirmed by Fourier transform infrared spectroscopy (FT-IR) (Figure S3 in the Supporting Information). According to thermal gravimetric analysis (TGA), the $SrCO_3$ starts to decompose at 650 °C (Figure 5). $SrCO_3$ usually decomposes at 850−1000 °C depending on the particle size and distribution.[10] It is interesting that the $SrCO_3$ can decompose at such a low temperature in the present study. The TGA result presents a weight gain accompanied with a broad exothermal peak below 650 °C, which reflects the formation of iron oxide. $SrCoO_{3-\delta}$ forms as a transient phase at 700 °C and then disappears at 800 °C, accompanying the formation of SFC. It is likely that the $SrCO_3$ can react with Fe_2O_3 and $SrCoO_{3-\delta}$ to form SFC. Such a reaction results in the decomposition of $SrCO_3$ occurring at lower temperature. The transition at around 800 °C can be ascribed to the reduction of Co^{3+} to Co^{2+}.

The electrocatalytic activity toward ORR on the cathode was evaluated by electrochemical impedance spectroscopy (EIS). The Pt modified SSC composite cathode (SSC-Pt) was fabricated by the infiltration of the $PtCl_2$ solution into theSSC scaffold, followed by heating at 800 °C for 1 h. Figure 6a shows the typical curves of the EIS results tested at 650 °C in air. The area specific resistance (ASR) of the pristine SSC cathode is 0.044 Ω cm^2 at 650 °C. Two partially overlapped arcs can be observed, indicating that at least two different electrode processes limit the oxygen reduction reaction. The presence of two partially overlapped peaks in the Bode plots confirms two processes are involved in the ORR on the pristine SSC cathode (Figure 6b). In our previous study, for SSC, we confirmed that the arc at high frequency is related to the charge-transfer process, while the one at low frequency is related to the surface diffusion of oxygen atoms or the adsorption of molecular oxygen.[11] The charge-transfer process is the rate-determining step for ORR on SSC as a result of the relatively low electrical conductivity of SSC. For amorphous iron oxide or platinum modified SSC cathodes, both processes are optimized pronouncedly and the low-frequency arc disappeared on the SSC-Pt cathode. Figure 7 shows the dependence of ASRs on the temperature for the pristine SSC, SSC-Fe, and SSC-Pt cathodes. The decoration of

dx.doi.org/10.1021/cm201439d |*Chem. Mater.* 2011, 23, 4193–4198

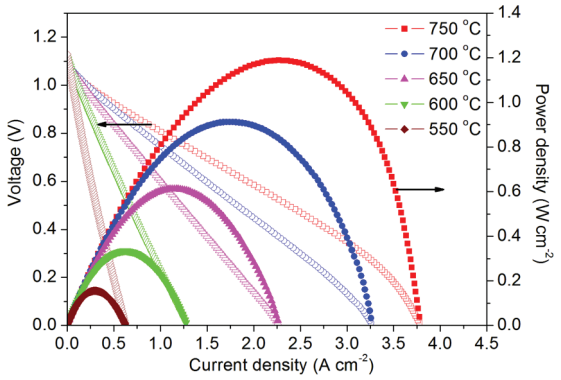

Figure 8. $I-V$ and $I-P$ curves of the complete cell based SSC-Fe cathode.

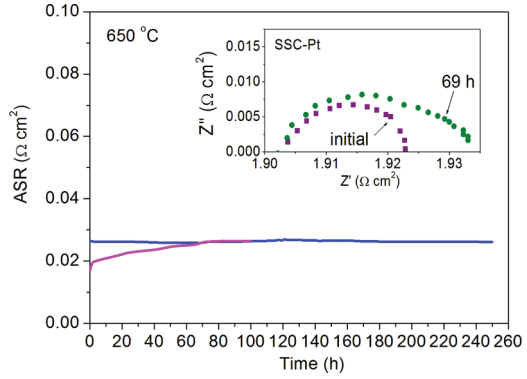

Figure 9. Comparison of stability of SSC-Fe decorated SSC-Pt at 650 °C. (Inset, the change of EIS on SSC-Pt after 69 h, indicating the sintering of the Pt catalysts.)

amorphous iron oxide pronouncedly reduces the ORR resistance. For example, the ASRs of the SSC-Fe cathode are only 50 and 54% that of the pristine SSC at 700 and 650 °C, respectively, which are comparable to those of the SSC-Pt one.

The performance of the SSC-Fe cathode for ORR in SOFC was further evaluated with a YSZ-Ni (50:50 vol %) anode supported SDC(~5 μm)|YSZ(~10 μm) electrolyte single cell. YSZ is the most popular electrolyte for the commercialization of SOFC because of its advantages of mechanical robustness and negligible electronic conduction at high temperature. Therefore, we adopted YSZ as the electrolyte for the single cell in this study. To prevent the phase reaction between the cathode and electrolyte during fabrication and operation, an SDC thin film was used between SSC and YSZ. Figure 8 shows the current−voltage ($I-V$) and the corresponding power density ($I-P$) curves. The open circuit voltages (OCVs) are 1.08, 1.09, 1.11, and 1.12 V at 750, 700, 650, and 600 °C, respectively, which are close to the predicted values from the Nernst equation. The maximum power densities (P_{max}) are 1188, 912, 612, and 335 mW cm^{-2} at 750, 700, 650, and 600 °C, respectively. The observed power densities are much higher than those delivered from the fuel cell based on the pristine SSC cathode (Figure S4 in the Supporting Information).

Stability is another important factor concerning the practical application. One of the disadvantages of noble metal catalysts is their sintering at high temperature. We compared the long-term stability of the SSC-Fe cathode to that of the SSC-Pt cathode. The SSC-Pt cathode shows lower ASR than SSC-Fe at the beginning. However, the ASR of SSC-Pt starts to increase after just 30 min and keeps increasing up to 0.026 Ω cm^2 at 69 h (Figure 9). On the basis of the EIS test, the resistance at low frequency increases, indicating the degradation of oxygen surface processes caused by the sintering of Pt particles (Figure 4c). For the SSC-Fe cathode, the ASR remains around 0.025 Ω cm^2 for 250 h without any degradation.

CONCLUSIONS

In summary, we have developed an amorphous iron oxide modified SSC cathode via CVD using ferrocene as the precursor. This novel cathode shows a 3D heterostructure with significantly improved electrocatalytic activity and excellent stability in the ORR at IT. The low cost for the iron oxide catalyst makes this structured cathode even more practical for the widespread utilization of IT-SOFCs.

ASSOCIATED CONTENT

Supporting Information. ASRs of crystallized Fe_2O_3 decorated perovskite electrodes, HRTEM image of pristine SSC, FT-IR results, and $I-V$ and $I-P$ curves for the single fuel cell based on a pristine SSC cathode. This material is available free of charge via the Internet at http://pubs.acs.org.

AUTHOR INFORMATION

Corresponding Author
*Fax: (+)61 7 3365 3528. E-mail: z.zhu@uq.edu.au.

ACKNOWLEDGMENT

W.Z. appreciates the support of an Australian Research Council (ARC) Discovery Project (Grant No. DP1095089).

REFERENCES

(1) Steel, B. C. H.; Heinzel, A. *Nature* **2001**, *414*, 345–352. Singhal, S. C. *Solid State Ionics* **2000**, *135*, 305. Shao, Z. P.; Zhang, C. M.; Wang, W.; Su, C.; Zhou, W.; Zhu, Z. H.; Park, H. J.; Kwak, C. *Angew. Chem., Int. Ed.* **2011**, *50*, 1792. Hibino, T.; Hashimoto, A.; Inoue, T.; Tokuno, J.; Yoshida, S.; Sano, M. *Science* **2000**, *288*, 2031. Liu, Q.; Dong, X. H.; Xiao, G. L.; Zhao, F.; Chen, F. L. *Adv. Mater.* **2010**, *22*, 5478.

(2) Shao, Z. P.; Haile, S. M. *Nature* **2004**, *431*, 170. Yang, L.; Zuo, C. D.; Wang, S. Z.; Cheng, Z.; Liu, M. L. *Adv. Mater.* **2008**, *20*, 3280. Zhou, W.; Sunarso, J.; Chen, Z. G.; Ge, L.; Motuzas, J.; Zou, J.; Wang, G. X.; Julbe, A.; Zhu, Z. H. *Energy Environ. Sci.* **2011**, *4*, 872. Dieterle, L.; Bockstaller, P.; Gerthsen, D.; Hayd, J.; Ivers-Tiffée, E.; Guntow, U. *Adv. Energy Mater.* **2011**, *1*, 249. Zhou, W.; Ran, R.; Shao, Z.; Jin, W.; Xu, N. *J. Power Sources* **2008**, *182*, 24. Zhou, W.; Shao, Z. P.; Ran, R.; Jin, W. Q.; Xu, N. P. *Chem. Commun.* **2008**, 5791–5793.

(3) (a) Vohs, J. M.; Gorte, R. J. *Adv. Mater.* **2009**, *21*, 943–956. (b) Jiang, Z. Y.; Xia, C. R.; Chen, F. L. *Electrochim. Acta* **2010**, *55*, 3595–3605.

(4) Lefèvre, M.; Proietti, E.; Jaouen, F.; Dodelet, J.-P. *Science* **2009**, *324*, 71–74. Yuasa, M.; Yamaguchi, A.; Itsuki, H.; Tanaka, K.; Yamamoto, M.; Oyaizu, K. *Chem. Mater.* **2005**, *17*, 4278–4281. Maruyama, J.; Abe, I. *Chem. Commun.* **2007**, 2879–2881.

(5) Hou, S.; Alonso, J. A.; Rajasekhara, S.; Martinez-Lope, M. J.; Fernandez-Diaz, M. T.; Goodenough, J. B. *Chem. Mater.* **2010**, *22*, 1071–1079.

(6) Machala, L.; Zboril, R.; Gedanken, A. *J. Phys. Chem. B* **2007**, *111*, 4003–4018.

(7) Fjellvåg, H.; Hauback, B. C.; Bredesen, R. *J. Mater. Chem.* **1997**, *7*, 2415–2419. Pardo, J. A.; Santiso, J.; Solís, C.; Garcia, G.; Figueras, A.; Rossell, M. D. *Solid State Ionics* **2006**, *177*, 423–428. Bredesen, R.; Norby, T.; Bardal, A.; Lynum, V. *Solid State Ionics* **2000**, *135*, 687–697.

(8) Jose laO', G.; Ahn, S.-J.; Crumlin, E.; Orikasa, Y.; Biegalski, M. D.; Christen, H. M.; Shao-Horn, Y. *Angew. Chem., Int. Ed.* **2010**, *49*, 5344–5347. Guo, X. X.; Maier, J. *Adv. Mater.* **2009**, *21*, 2619–2631. Sata, N.; Eberl, K.; Eberman, K.; Maier, J. *Nature* **2000**, *408*, 946–949. Infortuna, A.; Harvey, A. S.; Gauckler, L. J. *Adv. Funct. Mater.* **2008**, *18*, 127–135.

(9) Zhou, W.; Ran, R.; Shao, Z. P. *J. Power Sources* **2009**, *192*, 231–246. Yan, A.; Cheng, M.; Dong, Y.; Yang, W.; Maragou, V.; Song, S.; Tsiakaras, P. *Appl. Catal., B* **2006**, *66*, 64–71.

(10) Zhou, W.; Shao, Z. P.; Ran, R.; Gu, H. X.; Jin, W. Q.; Xu, N. P. *J. Am. Ceram. Soc.* **2008**, *91*, 1155–1162.

(11) Zhou, W.; An, B. M.; Ran, R.; Shao, Z. P. *J. Electrochem. Soc.* **2009**, *156*, B884–B890. Zhou, W.; Shao, Z. P.; Ran, R.; Cai, R. *Electrochem. Commun.* **2008**, *10*, 1647–1651.